Physica Scripta

PAPER • **OPEN ACCESS**

Space-resolved line shape model for sputtered atoms of finite-size targets

To cite this article: M Sackers *et al* 2023 *Phys. Scr.* **98** 115603

View the article online for updates and enhancements.

You may also like

- Sputtering and redeposition of ion irradiated Au nanoparticle arrays: direct comparison of simulations to experiments
Henry Holland-Moritz, Andrey Ilinov, Flyura Djurabekova et al.
- Effect of voltage pulse characteristics on high-power impulse magnetron sputtering of copper
Tomáš Kozák and Jaroslav Vlek
- Transition from ballistic to thermalized transport of metal-sputtered species in a DC magnetron
Adrien Revel, Abderzak El Farsy, Ludovic de Poucques et al.

This content was downloaded from IP address 134.94.122.118 on 26/10/2023 at 10:10

Physica Scripta

PAPER

Space-resolved line shape model for sputtered atoms of finite-size targets

M Sackers , O Marchuk , S Ertmer , S Brezinsek and A Kreter

Forschungszentrum Jülich GmbH, Institut für Energie- und Klimaforschung–Plasmaphysik, Partner of the Trilateral Euregio Cluster (TEC), 52425 Jülich, Germany

E-mail: m.sackers@fz-juelich.de

Keywords: low-density plasma, energy distribution, angular distribution, sputtering, finite-size target, spectroscopy

OPEN ACCESS

RECEIVED
9 June 2023

REVISED
2 September 2023

ACCEPTED FOR PUBLICATION
28 September 2023

PUBLISHED
9 October 2023

Original content from this work may be used under the terms of the Creative Commons Attribution 4.0 licence.

Any further distribution of this work must maintain attribution to the author(s) and the title of the work, journal citation and DOI.

Abstract

High-resolution emission spectroscopy provides valuable information on the physical sputtering process during plasma-wall interaction. Up to now, analyzing the observed spectral lines during sputtering did not account for the finite size of the targets. It becomes crucial if the size of the target becomes comparable with the distance the sputtered atoms travel before emitting the photons. So, for example, the generally used standard emission model based on an infinite target or the point source approximation breaks for observations using two lines of sight: parallel and perpendicular to the normal of the target. It is impossible to achieve consistent results for energy and angular distribution of sputtered atoms. The new space-resolved emission model for finite-size targets developed in this work removes this gap. It incorporates the space-velocity transformation for the distribution function and includes the finite lifetime of excited states. The model was validated using emission spectra of sputtered atoms from a polycrystalline tungsten sample bombarded by monoenergetic Ar^+ with kinetic energies of 100 eV to 140 eV at normal incidence in the linear plasma device PSI-2. Using the new model enables the simultaneous fitting of the line shapes of sputtered tungsten for both observation angles. The optimization process is performed using the standard Thompson distribution by separating the energy-dependent parameter and the angular distribution.

1. Introduction

Sputtering is the fundamental process of plasma-surface interaction in many kinds of laboratory plasmas, plasma chemistry, or, finally, in thermonuclear fusion [1–4]. It strictly limits the possible operating scenarios for applications where it erodes crucial components or leads to radiative cooling of the plasma. For instance, in magnetic fusion, sputtering limits the lifetime of the wall material and negatively impacts the impurity concentration in the plasma core through the accumulation of high Z impurities [5]. Likewise, the performance of Hall thrusters used for spacecraft propulsion degrades over time via erosion of crucial components [6]. At the same time, physical sputtering offers a compelling way to produce high-quality coatings, as it is possible to build up the deposition atom by atom. Its utilization in low-temperature plasmas is known as magnetron sputtering discharges, which has found widespread use in industrial applications [7, 8]. Furthermore, the performance of diagnostic mirrors in fusion reactors, such as ITER and DEMO, is expected to be degraded by the formation of a significant amount of impurity deposition. As a possible solution for *in situ* cleaning, controlled low-temperature discharges that remove thin deposition films gained rising interest [3, 9, 10].

The origins of modern-day sputtering theory can be traced back to an experiment by G. H. Wehner, which clarified whether or not sputtering occurs due to the heating of the material and its sublimation according to the Knudsen Cosine law or by collisional cascades [11, 12]. His main idea was to irradiate monocrystalline targets with low-energy ions and to analyze the deposition pattern on a glass plate. He found spot-like structures that

© 2023 The Author(s). Published by IOP Publishing Ltd

clearly depend on the surface orientation of the crystal, verifying collisional cascades as the dominant process in physical sputtering.

This discovery stimulated flourishing theoretical investigations on sputtering. In particular, Sigmund made considerable contributions and Thompson derived a frequently used formula to describe the flux of sputtered particles [13, 14]. Important parameters describing the physical sputtering process are the sputtering yield, the velocity and angular distribution of sputtered particles [15]. The velocity distribution is accessible by a wide range of experimental methods. For instance, irradiating a sample using an ion beam and then detecting laser-induced fluorescence (LiF) probes this distribution function [16–19]. Considerable variations of time-of-flight techniques exist as well. They rely on pulsing the beam of bombarding projectiles followed by deposition on a rotating surface [20, 21], detection in a quadrupole mass spectrometer [22] or excitation in plasma and time-resolved measurements of the emission [23, 24]. A plasma may also provide substantial ionization to sputtered particles to probe the energy distribution function (EDF) using a retarding field analyzer [25].

At linear plasma devices, such as PSI-2, or in magnetron sputtering discharges, high-resolution emission spectroscopy, laser absorption spectroscopy and laser-induced fluorescence resolve the shape of the radiative transitions by sputtered atoms [26–29]. Also, the measurements of polarization properties of metallic mirrors using emission properties of the backscattered atoms rely on the theoretical description of the measured line shapes [30]. The most generally used model is that of an infinite target or the point source approximation (ITA) [17, 19, 31]. Regarding the line of sight parallel to the normal, there exists a model that accounts for the finite size of the target [32, 33]. These models originated in the early 1980s when computational resources were scarce, such that they provided analytical formulas that worked well for high-energy sputtering. Their validity degenerates for experiments approaching the near-threshold sputtering regime since energy conservation was violated while deriving the analytical formulas.

Measuring emission spectra at PSI-2 and their analysis was restricted in previous campaigns to the line of sight (LOS) parallel to the normal of the target. Adding the LOS perpendicular to the normal and analyzing both spectra using the same angular and velocity distribution in the numerical ITA proved impossible as the line shape for both LOS could not be modeled consistently. To our knowledge, a model that correctly captures the line shape for the LOS perpendicular to the normal does not exist yet. This work provides the proper framework for transforming the distribution functions so that their numerical evaluation is straightforward for both observation angles.

This work is structured in the following way: First, section 2 presents the experimental setup, followed by section 3, which introduces the general line-broadening mechanisms for sputtered atoms and then focuses on deriving the space-resolved emission model for finite-size targets in local and velocity space. Section 3.2 compares the new model to the ITA and illustrates the dependency of the line shape for the LOS parallel and perpendicular to the normal on the energy and angular distribution function (ADF). Finally, section 4 validates the new model using emission spectra of the 498 nm W I resonant line of sputtered tungsten obtained at PSI-2 for sputtering by ions at normal incidence. For that purpose, a polycrystalline tungsten sample was subjected to bombardment by monoenergetic Ar^+ with kinetic energies of 100 eV to 140 eV.

2. Linear plasma device PSI-2 and the spectroscopy setup

The linear plasma device PSI-2 generates a continuous plasma by igniting an arc discharge between a cylindrical cathode and anode [34]. This geometry allows performing spectroscopic measurements through the aperture. An axial magnetic field of about 100 mT confines the plasma and guides it onto samples for studying plasma-wall interaction. The potential difference between the target and plasma accelerates the ions. Thus, applying a bias to the target allows controlling the impact energy of the ion beam, which is essentially monoenergetic as the Debye screening length is much smaller than the mean free path of the ions. The axial magnetic field further ensures the bombardment of the sample at normal incidence [35]. The typical peak ion flux density onto the target during the argon discharges was about $3.3 \cdot 10^{21}$ $m^{-2}s^{-1}$ at a pressure of 0.03 Pa. Figure 1(b) presents the plasma parameters measured by the Langmuir probe, which is approximately one meter closer to the plasma source than the target. The spectrometer used in this study is in a high spectral order on an Echelle grating, which gives, in the case of the 498 nm line, a typical instrumental FWHM of 4.26 pm. The lines of sight parallel and perpendicular to the normal of the target are indicated in figure 1 by orange colored lines. A previous campaign involved an imaging spectrometer to measure the decay length of emission by sputtered W atoms. These measurements at a bias of 80 eV indicate that most emission occurs within a limited region in front of the target, which extends about 12 mm in the axial direction [36].

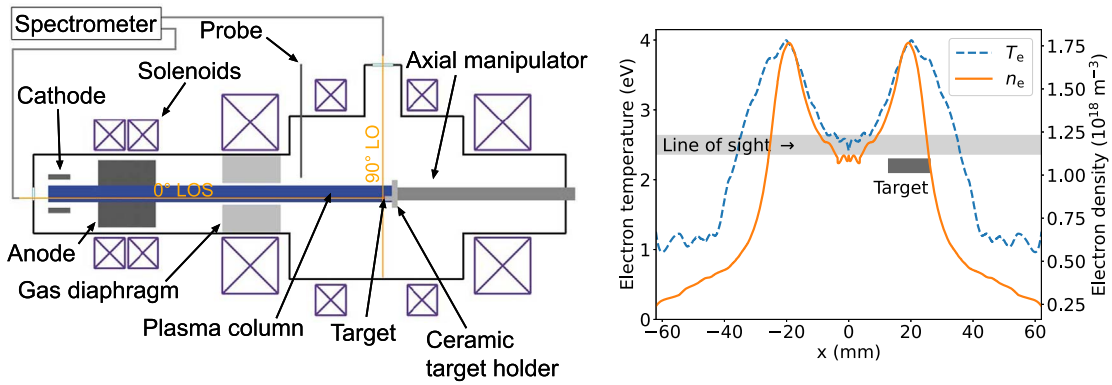

(a) Linear plasma device PSI-2 (b) Plasma parameters

Figure 1. Schematic overview of the linear plasma device PSI-2. The orange-colored lines are the two lines of sight of the spectrometer.

3. Optical emission spectroscopy of sputtered atoms

Various physical processes influence the line shape of transitions emitted by sputtered atoms. For example, the Zeeman and Stark effect shift the energy eigenvalues of the magnetic sublevels, which splits the line into discrete sub-transitions [37, 38]. A more continuous broadening is due to self-absorption, where the peak intensity is decreased relative to the wings of the line [39]. For most sputtering experiments, this is certainly not a dominant process, as the sputtered particles are essentially a minor impurity in the overall particle composition of the plasma. An exception may be the metal phases in HiPIMS discharges in which sputtered atoms may replace a significant part of the working gas [40].

The broadening of interest for this study is based on the well-known Doppler shift. Light emitted by particles passing through the detection volume of the spectrometer with a nonrelativistic velocity is observed at the shifted wavelength λ [39]:

$$\lambda = \lambda_0(1 - \mathrm{v}_{\mathrm{LOS}}/c), \tag{1}$$

with λ_0 the unshifted wavelength corresponding to the observed transition, $\mathrm{v}_{\mathrm{LOS}}$ is the projection of the velocity vector $\vec{\mathrm{v}}$ on the line of sight and c is the speed of light. Further accounting for the instrumental broadening $\mathcal{I}(\lambda)$ leads to the line profile [39, 41]

$$I(\lambda) \propto \mathcal{I}(\lambda) * \int_{\mathrm{LOS}} f_{\mathrm{u}}(l, \mathrm{v}_{\mathrm{LOS}}(\lambda))\,\mathrm{d}l, \tag{2}$$

where the distribution function of the upper-level f_{u} includes the remaining broadening mechanisms. Thus, measuring the line shape using a spectrometer with sufficient resolution can be an invaluable tool to probe the velocity distribution function of particles sputtered from a surface by plasma exposure.

3.1. Energy or velocity distribution function

The contribution to f_u by most of the broadening mechanisms is generally very straightforward. For example, [36] gives an example of treating the Zeeman effect. Particular attention has to be paid to the Doppler effect, which is essentially the velocity distribution function (VDF) of the sputtered particles (equation (1)). In literature, the distribution function of sputtered particles is generally given as a function of energy. Of the various EDFs that capture the sputtering kinetics for different combinations of target atom and projectile [13, 14, 42, 43], a modified version of the commonly used Thompson distribution

$$\Phi(E, \Omega, s, b) = \underbrace{\frac{E}{(E+E_b)^s}\left(1-\sqrt{\frac{E+E_b}{E_{\max}+E_b}}\right)}_{F(E,s)} \underbrace{\cos^b\theta}_{G(\Omega,b)} \tag{3}$$

is chosen, with E_{b} being the surface binding energy, s is the fitting parameter of the energy distribution, b is the parameter of the angular distribution θ of sputtered atoms where Ω is the solid angle with $\mathbf{d}\Omega = \mathrm{d}\phi\,\sin(\theta)\mathrm{d}\theta$ and $E_{\max}$ is the maximal kinetic energy of the sputtered atom [13]. According to Sanders [44], the maximal kinetic energy of the sputtered atom is:

$$E_{\max} = 4\frac{M_1 \cdot M_2}{(M_1 + M_2)^2}E_{\mathrm{imp}} - E_{\mathrm{b}}, \tag{4}$$

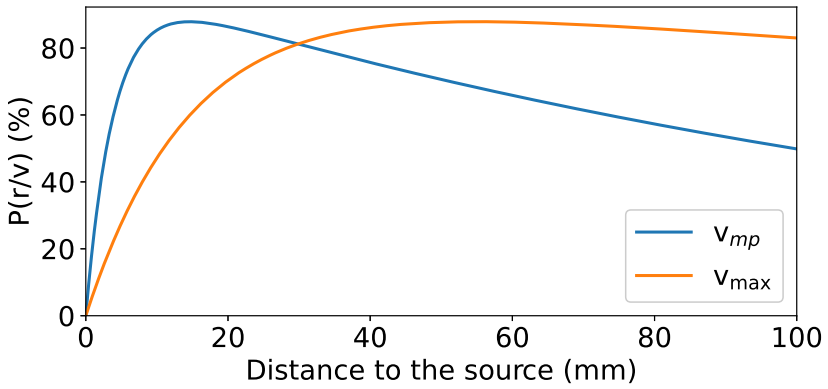

Figure 2. Intensity evolution of the resonant 498 nm W I transition neglecting the angular distribution. Parameters used: E_b = 8.68 eV [15], E_{imp}=120 eV, $\tau_{rad} = 1.9 \cdot 10^{-6}$ s [50]. Equation (4) yields a maximal kinetic energy of 61.69 eV. The ionization rate $n_e \langle \sigma v \rangle = 1/\tau_{iz}$ is calculated using the rate coefficient of Steinbrink [51, 52] for an electron temperature of 3.7 eV and assuming an electron density of $1.75 \cdot 10^{18}$ m^{-3} (cf figure 1(b)).

with $M_{1,2}$ being the mass of the projectile and target atom, respectively. Setting $s = 3$ and $b = 1$ in equation (3) yields the standard Thomson distribution. For low energies the angular distribution may differ substantially from the cosine one. Alternative angular distributions are undercosine (b < 1), overcosine (b > 1), or even heart-shaped [45, 46].

The elementary flux dS of particles leaving the surface with the solid angle Ω within the angle dΩ equals

$$\mathrm{d}S \propto \Phi(E, \Omega, s, b)\mathrm{d}E\mathrm{d}\Omega, \tag{5}$$

so that the total flux is

$$S = \int\int F(E, s)G(\Omega, b)\mathrm{d}E\mathrm{d}\Omega. \tag{6}$$

However, the spectrometer collects photons due to radiative decay of an excited electronic state, which depends linearly on the particle density

$$f(\mathrm{v}) = \Phi(\mathrm{v})/\mathrm{v}. \tag{7}$$

Further using [47] $\Phi(E, \Omega)\mathrm{d}E\mathrm{d}\Omega = \Phi(\mathrm{v}, \Omega)m\mathrm{v}\mathrm{d}\mathrm{v}\mathrm{d}\Omega$ provides the upper level density as

$$f_u(\mathrm{v}, \Omega) \propto F(E, s)G(\Omega, b)m. \tag{8}$$

Then, by omitting the square root term of equation (3) and setting $s = 3$, the most probable velocity ($\mathrm{v_{mp}}$) in spherical coordinates is [15]

$$\mathrm{v_{mp}} = \sqrt{E_b/m}. \tag{9}$$

Another crucial aspect is the time dependency of the upper-level density. For example, spectroscopic time of flight measurements applied during the sputtering of tungsten at the linear plasma device PSI-2 suggests that, for targets at room temperature, the sputtered particles leave the surface in the ground state [48]. Collisional-radiative processes determine the evolution of the population densities of the various atomic states: In low-density plasmas, levels that are directly radiatively coupled to the ground state via resonant transitions reach their equilibrium state in the timescale determined by their radiative lifetime [49]. Their coupling to metastable levels is generally less pronounced and, here, assumed to be negligible. It is well-known that plasmas generated at PSI-2 exhibit a hollow electron density and temperature profile due to the geometry of the source [34]. An estimate of its influence on the line shape is provided in section 4.1. In the following, the physics is kept as simple as possible to highlight the changes in line shape induced by including the finite size of the target when analyzing emission spectra. Thus, neglecting gradients in the excitation and ionization rates leads to the analytical solution of the line intensity evolution of

$$P(t) = (1 - \exp\{-t/\tau_{rad}\})\exp\{-t/\tau_{iz}\}, \tag{10}$$

where $\tau_{rad} = 1/\sum_l A_{ul}$ is the lifetime of the upper level u, A_{ul} is the transition probability between the levels u and l, and τ_{iz} is the lifetime of the neutral particle with respect to ionization. It is more convenient to express t in terms of r/v to estimate if this factor has to be included in the model. Equation (4) provides the maximal velocity of the sputtered atom, equation (9) gives the most probable velocity, and figure 2 presents the evaluation of equation (10) for distances of up to 100 mm to the source for sputtering of W by Ar^+ with an impact energy of 120 eV. Without a doubt, proper analysis of emission spectra from experiments at PSI-2 (13 mm x 13 mm target) or typical laboratory magnetron sputtering devices should account for the finite lifetime of exited levels by

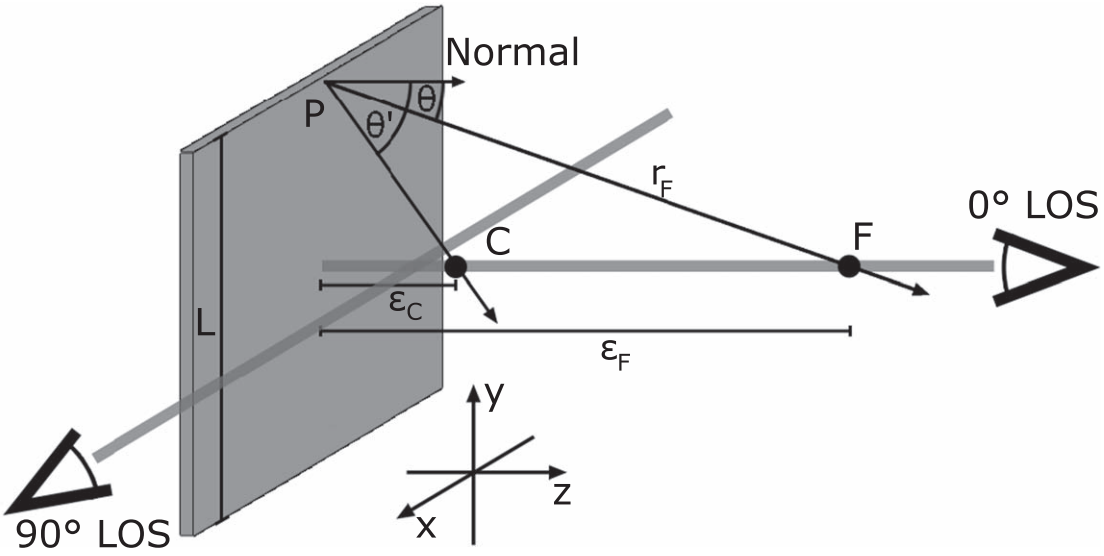

Figure 3. Lines of sight considered in this study and representation of the chosen Cartesian coordinate system. 0° and 90° correspond to the LOS parallel and perpendicular to the normal.

introducing factor (10) into equation (8):

$$F(\mathrm{v},\, s)G(\Omega,\, b)m\mathrm{dvd}\Omega \rightarrow F(\mathrm{v},\, s)P(r/\mathrm{v})G(\Omega,\, b)m\mathrm{dvd}\Omega. \tag{11}$$

3.1.1. Infinite-size target

The most straightforward case is encountered in LiF experiments since it is possible to construct a relatively small emission volume directly in front of the target. These conditions may be referred to as an infinite target approximation (ITA) or a point source approximation from which all light is collected [53]. For these cases, M. J. Pellin *et al* and R. B. Wright *et al* performed extensive work, providing analytical solutions for the VDFs in the Doppler-shifted direction parallel and perpendicular to the normal [17–19].

The numerical approach for lines of sight parallel and perpendicular to the normal, as shown in figure 3, begins with choosing a proper coordinate system. Cartesian coordinates in velocity space (v_x, v_y, v_z) fulfill the requirements of describing a quadratic source excellently due to having an axis parallel and perpendicular to the normal.

Accounting for the transformation between the spherical and Cartesian coordinate system in the velocity space and the expression for the polar angle gives the well-known result:

$$\mathrm{v}^2\mathrm{dvd}\Omega = \mathrm{dv}_x\mathrm{dv}_y\mathrm{dv}_z \tag{12}$$

The right-hand-side of the expression (11) becomes:

$$\frac{F(\mathrm{v},\, s)}{\mathrm{v}^2}P(r/\mathrm{v})G(\mathrm{v}_x,\, \mathrm{v}_y,\, \mathrm{v}_z,\, b)m\mathrm{dv}_x\mathrm{dv}_y\mathrm{dv}_z. \tag{13}$$

The last formula (13) determines the number of photons detected at the spectrometer at an arbitrary line of sight due to the flux of particles originating from the point (P), as shown in figure 3. The signal from different points at the surface appears at other wavelengths due to the Doppler shift. So, for instance, to determine the signal detected in the direction parallel to normal $\mathrm{v}_{\mathrm{LOS}} = \mathrm{v}_z$, integrating through the v_x and v_y coordinates is necessary. Analogously, performing the integration over the v_y and v_z components gives the signal in the x-direction ($\mathrm{v}_{\mathrm{LOS}} = \mathrm{v}_x$).

$$f_{\mathrm{u}}(\mathrm{v}_z) \propto \int\int P(\mathrm{r}/\mathrm{v})\frac{F(\mathrm{v},\, s)}{\mathrm{v}^2}G(\mathrm{v},\, b)\mathrm{dv}_x\mathrm{dv}_y \tag{14}$$

$$f_{\mathrm{u}}(\mathrm{v}_x) \propto \int\int P(\mathrm{r}/\mathrm{v})\frac{F(\mathrm{v},\, s)}{\mathrm{v}^2}G(\mathrm{v},\, b)\mathrm{dv}_z\mathrm{dv}_y. \tag{15}$$

The exact analytical solution[1] as in [17] are accessible by dropping the term $P(\mathbf{r}/\mathbf{v})$ that accounts for the excitation kinetics and by setting $s = 3$ and $b = 1$:

[1] We point out that the analytical expression shown in [18] conserves the number of particles and not the flux at the plasma surface. The flux conservation solution at the surface produces a more complicated form compared to [18].

$$f(\mathrm{v}_z) \propto \int_{-\infty}^{\infty}\int_{-\infty}^{\infty} \frac{1}{(\mathrm{v}_x^2+\mathrm{v}_y^2+\mathrm{v}_z^2+\mathrm{v}_b^2)^3}\frac{\mathrm{v}_z}{\sqrt{\mathrm{v}_x^2+\mathrm{v}_y^2+\mathrm{v}_z^2}}\mathrm{d}\mathrm{v}_x\mathrm{d}\mathrm{v}_y \tag{16}$$

$$f(\mathrm{v}_x) \propto \int_{-\infty}^{\infty}\int_{-\infty}^{\infty} \frac{1}{(\mathrm{v}_x^2+\mathrm{v}_y^2+\mathrm{v}_z^2+\mathrm{v}_b^2)^3}\frac{v_z}{\sqrt{\mathrm{v}_x^2+\mathrm{v}_y^2+\mathrm{v}_z^2}}\mathrm{d}\mathrm{v}_y\mathrm{d}\mathrm{v}_z \tag{17}$$

Convolving the functions f with the instrumental profile finally provides the synthetic line shape. This output is then compared with the measurements. One crucial result is that the expressions ((16)–(17)) are independent of the position from where the emission originates along the line of sight. Thus, simulating the spectrum originating from one point within the LOS provides the complete solution.

3.1.2. Finite-size target

In general, the finite size of the target plays a pivotal role in the analysis of emission spectra by atomic species eroded during plasma operation. Figure 3 illustrates such a case. If for point C $\epsilon_C \ll L$, the ITA approximation remains valid as the particles emitted at arbitrary angle θ contribute to emission, the situation changes for the point F due to $\epsilon_F >> L$. It boils down to the fact that the angular width $\Delta\Omega$ covered by the target decreases for positions further away from it. Essentially the particles emitted at the large azimuthal angle ($\theta \rightarrow \pi/2$) would not be observed in the spectra *a priori*. As a result, the line shape obtained by an ITA analysis is not adequate to model such data. The new space-resolved model (SRM) addresses these inconsistencies by including the finite size of the target and the lifetime of excited levels of atoms.

The elements of the SRM are given below. The unit vectors of the velocity of the particle ($\mathbf{n}_\mathrm{v}$) and the radial direction from the source to the emission positions ($\mathbf{n}_\mathrm{r}$) coincide such that the projection of the total velocity onto the line of sight is given by

$$\mathrm{v}_{\mathrm{LOS}} = \mathrm{v}\ \mathbf{n}_\mathrm{r}\cdot\mathbf{n}_{\mathrm{LOS}}, \tag{18}$$

with $\mathbf{n}_{\mathrm{LOS}}$ the unit vector in the Doppler-shifted direction. Using this relation, the VDF is converted into the Doppler-shifted VDF via

$$F(\mathrm{v})\frac{\mathrm{d}\mathrm{v}}{\mathrm{d}\mathrm{v}_{\mathrm{LOS}}}\mathrm{d}\mathrm{v}_{\mathrm{LOS}} = \frac{F(\mathrm{v}_{\mathrm{LOS}})}{\mathbf{n}_r\cdot\mathbf{n}_{\mathrm{LOS}}}\mathrm{d}\mathrm{v}_{\mathrm{LOS}}. \tag{19}$$

As the surface lies in the x-y plane, the transformation of the surface element is given by

$$G(\Omega)\mathrm{d}\Omega = G(\theta,\ \phi)\sin\theta\mathrm{d}\theta\mathrm{d}\phi = G(\mathbf{r})\frac{\sqrt{x^2+y^2}}{\sqrt{x^2+y^2+z^2}}\left|\frac{\partial(\theta,\ \phi)}{\partial(x,\ y)}\right|\mathrm{d}x\mathrm{d}y \tag{20}$$

This Jacobian determinant evaluates to

$$\frac{\sqrt{x^2+y^2}}{\sqrt{x^2+y^2+z^2}}\left|\frac{\partial(\theta,\ \phi)}{\partial(x,\ y)}\right| = \frac{z}{r^3}, \tag{21}$$

where $r = \sqrt{x^2+y^2+z^2}$. The result is consistent with investigations on deposition thickness in magnetron sputtering where, in essence, only a different moment ($\phi = \iint f(v)v\mathrm{d}^3v$) of the distribution function is investigated [4, 54, 55]. For the following, the location of the point considered in the line of sight corresponds to the origin of the coordinate system. Thus, the center of the target shall be at $-\bar{x}$, $-\bar{y}$, and $\bar{z}$ and extends from $-L_x/2-\bar{x}$ to $L_x/2-\bar{x}$ in the x-direction and from $-L_y/2-\bar{y}$ to $L_y/2-\bar{y}$ in the y-direction. Then, the direction along r coincides with the orientation of $-\mathrm{v}$ from the target to the point on the line of sight. Finally, integration over the surface of the target using equations (10), (19), and (20) provides the upper-level density:

$$f_{\mathrm{u}}(\mathrm{v}_{\mathrm{LOS}},\ \bar{x},\ \bar{y},\ \bar{z}) = \int_{-L_y/2-\bar{y}}^{L_y/2-\bar{y}}\int_{-L_x/2-\bar{x}}^{L_x/2-\bar{x}} P(r/\mathrm{v}(\mathrm{v}_{\mathrm{LOS}},\ \mathbf{r}))\frac{F(\mathrm{v}_{\mathrm{LOS}})}{\mathbf{n}_r\cdot\mathbf{n}_{\mathrm{LOS}}}G(r)\frac{\bar{z}}{r^3}\mathrm{d}x\mathrm{d}y, \tag{22}$$

with $\bar{x}$, $\bar{y}$ and $\bar{z}$ as the position shifted from the center of the target at which the emission takes place. L_x and L_y are the lengths of the quadratic target in the x- and y-direction, respectively. The final task is to integrate equation (22) along the LOS: It becomes evident that in the case of a finite target, the detected signal depends on the position $\bar{z}$ in front of the target. Similarly to the analytical formulas describing an infinite target, there exists an equation by Hintz *et al*, which treats the particle flux density of a finite target parallel to the normal [32], which is just a special case of treating equation (22).

Solving the problem in velocity space is possible for the LOS parallel and perpendicular to the normal. It is required to evaluate equations (14) or (15) at each position along the LOS while using proper bounds during the integration. Indeed, by expressing the distance the atoms travel through the velocity components as $\Delta y/\Delta z = \mathrm{v}_y/\mathrm{v}_z$ and $\Delta x/\Delta z = \mathrm{v}_x/\mathrm{v}_z$, one obtains the minimal and maximal velocities in the x- and y-direction respectively:

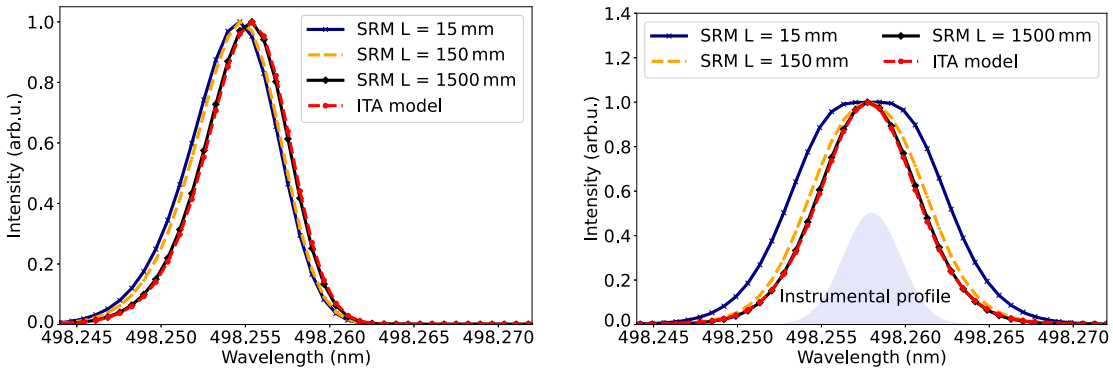

(a) Simulated spectra at 0° (b) Simulated spectra at 90°

Figure 4. Comparison of the ITA to the SRM for W bombarded by 120 eV Ar^+ assuming a standard Thompson distribution and a Gaussian instrumental broadening of 0.004 nm. The angular distribution is a cosine, the Z distance to the target for the LOS perpendicular to the normal is 2 mm, and the input into the model for calculating the SRM spectra differs solely concerning the size of the target.

$$v_{x,\min} = \frac{-L_x/2 - \overline{x}}{\overline{z}} v_z, \tag{23}$$

$$v_{x,\max} = \frac{L_x/2 - \overline{x}}{\overline{z}} v_z, \tag{24}$$

$$v_{y,\min} = \frac{-L_y/2 - \overline{y}}{\overline{z}} v_z, \tag{25}$$

$$v_{y,\max} = \frac{L_y/2 - \overline{y}}{\overline{z}} v_z. \tag{26}$$

Furthermore, the conservation of energy has to be fulfilled, leading to the additional condition:

$$v_{\max}^2 \geqslant v^2 = v_x^2 + v_y^2 + v_z^2. \tag{27}$$

To conclude, the evaluation of the integrals in local (equation (22)) or velocity space (equations (14) and (15)) using adequate constraints supplies the upper-level density needed to solve equation (2).

3.2. Comparison between the ITA and the SRM results at the experimental conditions of PSI-2 plasma

Before validating the space-resolved model (SRM) using experimental data, it is beneficial to investigate the general dependency of the synthetic spectra for both observation angles using the ITA and SRM methods. For that purpose, emission spectra of the W I 498 nm resonance line are simulated for the LOS parallel and perpendicular to the normal of a quadratic and planar tungsten target (13 mm x 13 mm). The integration paths chosen for these calculations coincide with those of the emission spectroscopy setup during plasma exposure at the PSI-2 facility. In the case of the line of sight parallel to the normal, the collecting length was about 1500 mm. This value corresponds to the distance between the hollow cathode of the plasma source and the target, as in the previous campaign [56]. Spectroscopic time-of-flight measurements at PSI-2 illustrate a fast decay of the W line emission at the z-axis distances of about 50 mm [36]. Similarly, the simulations suggest an integration length of 300 mm through the z-axis captures all significant contributions to the emission spectrum. In the direction perpendicular to the surface normal, the focus was positioned at the center of the target in the y-direction. The spot size of the optical setup in front of the target is about 3 mm and the distance in the z-direction between the LOS and the target is 2 mm. In the simulation, the integration length of 60 mm was selected, which corresponds approximately to the FWHM of the plasma profiles of PSI-2 plasma where the excitation process primarily occurs. Previous works introduced the ITA code [57, 58], the dominant broadening mechanisms [29], and the reflection of light at the target [30]. Figure 4 presents the results of calculating emission spectra using the SRM and ITA approaches. The output of the SRM simulations, as per formula (22), approaches the spectral profile generated with the ITA model from equations (14)–(15) if the target size increases and the time-dependent factor (equation (10)) is excluded. Figures 4(a) and (b) show the numerical comparison and line shape changes induced by accounting for the finite size of the target for the different lines of sight. The broadening by the external magnetic field is negligible for the 498 nm line as optical isolation and a linear polarizer allow the detection of an isolated Zeeman component [56]. The reflection of the target is also set to zero.

The differences in the line shape depending on treating the target in the ITA and SRM can be understood by analyzing figure 3. Given an emission volume much smaller than the size of the target ($\epsilon \ll L$) and a constant

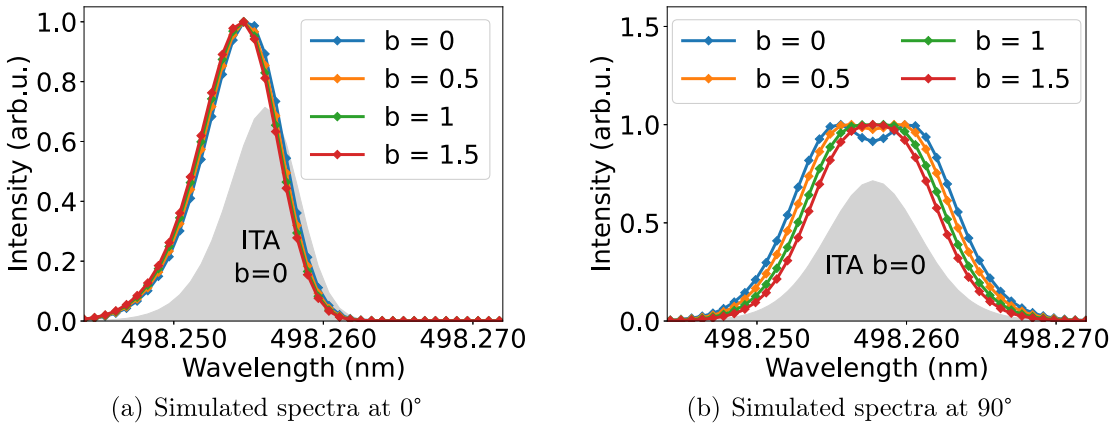

(a) Simulated spectra at 0° (b) Simulated spectra at 90°

Figure 5. Influence of angular distribution on the line shape for LOS parallel and perpendicular to the surface normal. The angular distribution is varied from an overcosine b=1.5 to an isotropic distribution $b = 0$. All other parameters of the SRM model and the experimental setup are consistent with those provided in the caption of figure 4.

relative population density of the upper level (cf equation (10)), ITA conditions are valid. All particles leaving the target with any possible velocity combination $\mathbf{v} = (v_{||z}, v_{\perp z})$ are represented in the emission volume, validating ITA approximation (14)–(15) for this case. In any other situation, some particles leaving the target surface cannot move into the emission volume. Most affected are particles having a high-velocity component perpendicular to the LOS compared to the parallel component ($v_{\perp z} > v_{||z}$). The loss of these particles depletes the low-velocity part of the distribution function in the LOS direction. This loss of particles leads to a much higher relative contribution of fast particles in the LOS direction, manifesting as an effective broadening of the line shape. For example, the spectrum shown in figure 4(a) exhibits increased blue-shifted emission for a finite target compared to an infinitely large target. Thus, the relative amount of particles with a high-velocity component in the direction of the LOS increases for a finite-size target.

3.3. Influence of energy and angular distribution on the line profile

The influence of the EDF, assuming an increase in energy, on the line shape can be explained as follows: In the case of the LOS parallel to the normal of the target, the higher velocity of the sputtered atoms increases the blue-shifted signal, as shown in figure 4(a). Analogously, for the LOS perpendicular to the normal, the very same reasoning applies. Here, the redshift increases as well. The influence of the ADF on the line shape is investigated by simulating spectra under variation of the power of the cosine distribution—isotropic ($b = 0$) to an over-cosine ($b = 1.5$). The results of these simulations are presented in figures 5(a) and (b).

For 90°, a decrease in b effectively broadens the spectrum, whereas, at 0°, the opposite trend is observed. This property should be no surprise as a larger off-normal angle corresponds to more particles having a high-velocity component perpendicular to the normal. Essentially, the average velocity parallel to the normal decreases, whereas the inverse occurs for the other observation angle. Worth pointing out is that even though the ADFs considered do not exhibit the heart-shaped distribution function, the emission profile shows a local minimum at the unshifted wavelength region as b approaches 0. The area shaded in grey presented in figure 5(b) is a profile generated using the ITA model for an isotropic ADF, which does not have the dip at the central wavelength. Thus the heart-shaped emission profile for the line of sight parallel to the target does not necessarily reflect the heart-shaped distribution function of sputtered atoms [45].

3.4. Impact of finite liftime on the line shape

Figure 2, shown in section 3.1, indicates that a constant upper-level density may not be appropriate for modeling the line shape accurately. Here, the lifetime of the atomic state determines the time that the upper level needs to reach equilibrium with the ground state. Neutral tungsten ionizes while it moves through the plasma, decreasing the density of the upper level. These two processes compete and lead to opposite effects on the line shape, as shown in figure 6, assuming homogeneous plasma parameters through the whole volume. The black lines in figures 6(a) and (b) correspond to simulations that neglected all effects of the finite lifetimes due to radiative decay and ionization. Accounting for radiative decay decreases the upper-level population density of fast-moving particles compared to slower ones such that the red-colored line does not exhibit as pronounced of a Doppler shift. On the other hand, ionization affects slow-moving particles more as they remain longer within the plasma before emitting the light detected by the spectrometer. Thus, ionization broadens the spectra.

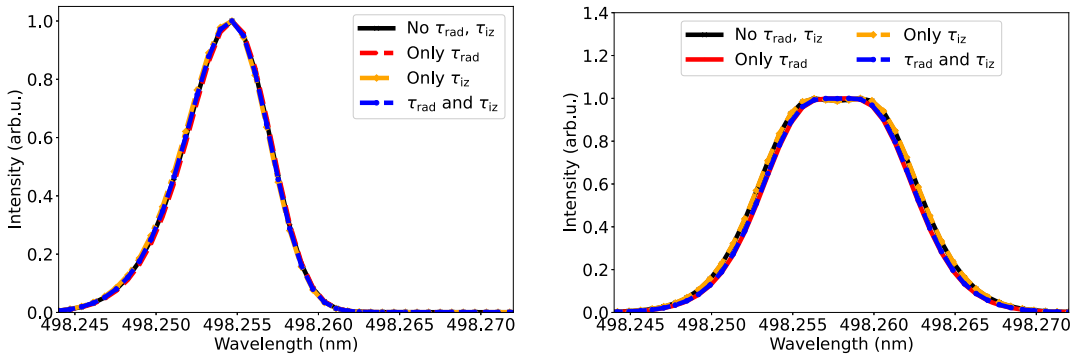

(a) Simulated spectra at 0° (b) Simulated spectra at 90°

Figure 6. Simulation of line shapes using the parameters consistent with those provided in the caption of figure 4. Excitation and ionization are considered for homogeneous plasma parameters.

Considering both effects gives the blue-colored line. The correction to the line shape, in this particular case, is very modest, especially when compared to those associated with the size of the target (cf figure 4).

4. Fitting of spectra obtained at the linear plasma device PSI-2

The previous section 3.3 illustrated the different behavior of the line shape concerning the LOS direction parallel and perpendicular to the normal on the angular distribution. This dependency of the spectra on the distribution function is the basis of an iterative fitting procedure for experimental data to obtain information on the EDF and ADF by optimizing s and b in equation (3). First, s is fitted using the 0° spectra, assuming $b = 1$. In this particular case, it is worthwhile to point out that sputtered particles emit light in the direction of the detector and the target. The reflectivity of the target, which depends on its surface condition and material composition, generates an asymmetry by providing a red-shifted signal [30, 59]. Next, the s value obtained in the first fit is fixed while optimizing the spectra at 90° using b as the free parameter. These two steps are repeated till the convergence of the fitting procedure. Figures 7(a)–(f) show the results of the SRM approach for experimental data obtained at the linear plasma device PSI-2 compared to the results obtained by optimizing the EDF using the ITA at 0° for a cosine angular distribution. The values of the energy distribution function parameter are presented in table 1.

Compared to previous work without optical isolation [29], there are slight differences in the optimal value of the EDF parameter s, assuming the ITA and fitting the spectra at 0° due to the isolation of a Zeeman component as described in [36, 56]. Previously using the ITA method for analyzing 0° spectra, the most substantial relative deviation of the fit compared to the experimental data was at the high energetic tail of the EDF—essentially at the wings of the direct and reflected emission [29]. However, optical isolation removed the blending of Zeeman components, which provides a higher resolution and reveals that even the dip in the center is not accurately modeled by ITA. However, it is impossible to adequately fit the experimental spectra obtained at the 90° LOS using the ITA. Even assuming an isotropic angular distribution ($b = 0$) is not sufficient to broaden the simulated spectra enough. Actually, this apparent paradox was the main reason for developing the SRM.

For both observation angles, the SRM captures the line profile significantly better. At 0°, the high-energetic tail of the emission spectrum is matched much more closely by the fit. Particularly important is that the experimental data for both directions are reproduced quite accurately by the same EDF and ADF parameters.

A clear trend is evident for the analysis using the SRM. The energy distribution parameter differs increasingly from the standard Thompson distribution value of $s = 3$ at lower impact energies. ACAT simulation by Yamamuara *et al* for the bombardment of Nb and Cu by Ar^+ yielded similar values, but they omitted the square root term in the Thompson distribution (equation (3)) [60]. Similarly, LiF data from [61] indicate that bombardment of tungsten by 300 eV Ar^+ at normal incidence cannot be described by a standard Thompson energy distribution and would require $s > 3$.

The ADF parameters obtained during this campaign indicate an undercosine distribution for bombarding W with Ar^+ having impact energies below 140 eV. It has not been attempted to optimize heart-shaped distribution functions to avoid overfitting the data. Experiments by other groups typically suggest heart-shaped distribution functions in this energy regime. For instance, a fixed quadrupole mass spectrometer combined with a rotatable target exposed to an rf plasma is one method used to gain information on the ADF [62]. The ADF, in this case, clearly seems to be heart-shaped [63]. These ADFs were used to model the decay behavior of various lines of W I at PSI-2 using the ERO code [64]. Similarly, bombarding a target with a small plasma beam at the

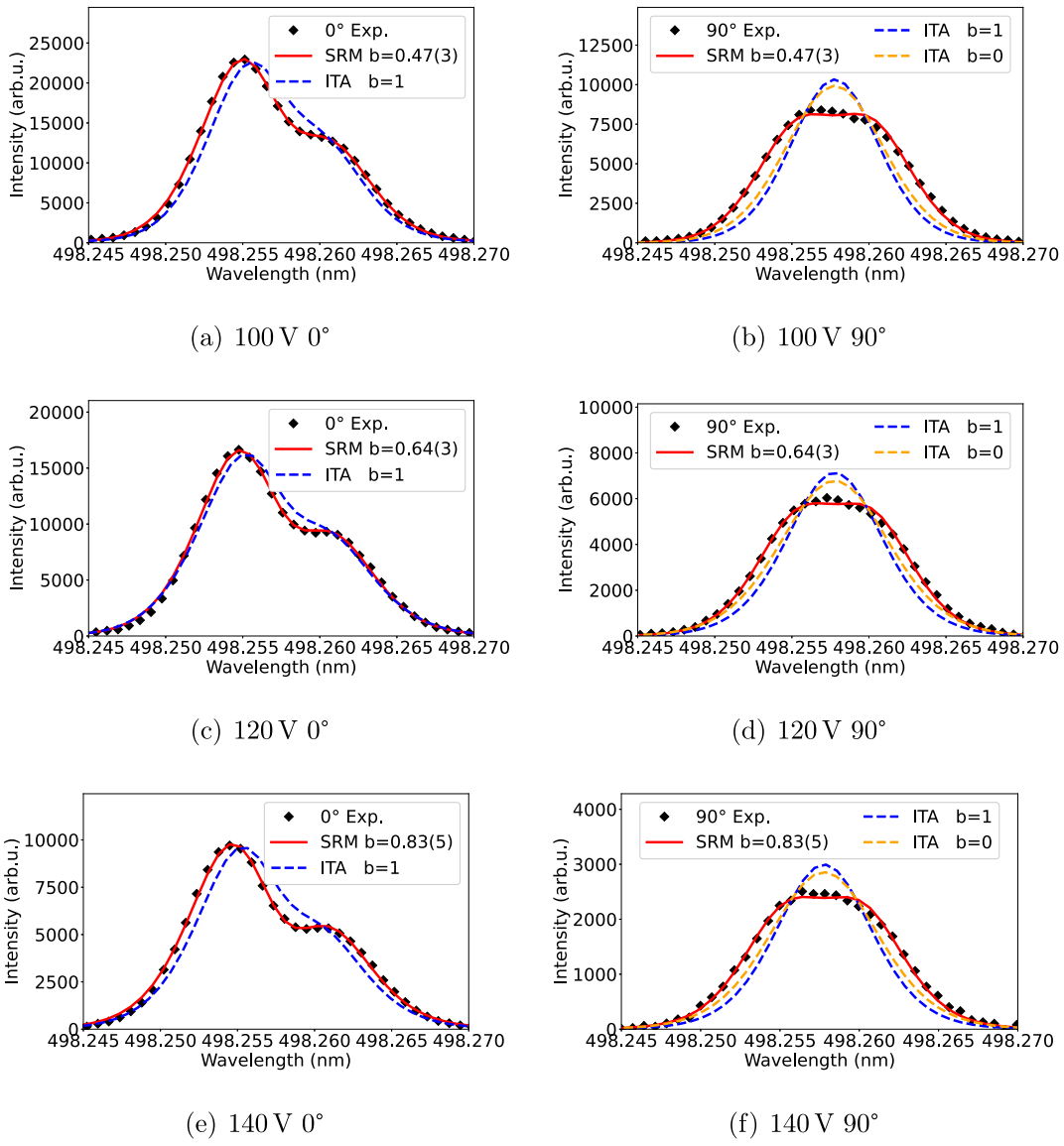

Figure 7. Experimental data for bombarding a W target with Ar^+ and fitting results. 0° and 90° correspond to the LOS parallel and perpendicular to the normal of the target, respectively.

Table 1. Parameters *s* and *b* of the energy and angular distribution function (3) obtained from the SRM and ITA methods for bombarding W with Ar ions at the linear plasma device PSI-2. SRM1 represents the results obtained by assuming constant excitation rate, whereas, in the case of SRM2, the excitation occurs only in front of the target and thus is described by a step function, as explained in section 4.1.

E_{kin} (eV)	100 eV		120 eV		140 eV	
	s	*b*	*s*	*b*	*s*	*b*
ITA	2.83(19)	1	2.31(6)	1	2.59(11)	1
SRM1	3.24(2)	0.47(3)	3.13(3)	0.64(3)	3.03(3)	0.83(5)
SRM2	3.05(3)	0.13(4)	2.99(4)	0.29(3)	2.92(3)	0.51(4)

PR-2 facility and collecting the sputtered particles as a deposition on a Cu surface gives an angular resolved measurement of the ADF [65]. The results of their work agree well with predictions from molecular dynamics simulations, which provide heart-shaped ADFs under these conditions.

4.1. Excitation profile in the radial direction

Electron density and temperature profiles measured by a Langmuir probe at the PSI-2 indicate significant gradients, which may influence the excitation kinetics. Figure 1(b) shows these profiles, the approximate position of the target, and the line of sight of the spectrometer. Atoms moving toward the spectrometer should experience more excitation than those in the opposite direction. This should yield a substantially larger blue-shifted component in the experimental data. However, the spectra shown in figure 7 exhibit an asymmetry of just a few percent. This can be understood by considering that for cosine-like distributions, most particles exiting the surface have a relatively small off-normal angle and thus move just through the excitation profile in front of the target. For very strong undercosine or heart-shaped distributions, the asymmetry should be much more pronounced.

Combining this reasoning with the peaked electron density and temperature profiles, motives to use a step profile for the excitation. In this case, an atom travels for a time of $t_1 = r_1/v$ through the excitation volume, which is, again, described by equation (10). During the remaining transit time t_2, the atom experiences exclusively radiative decay, so its density decreases by

$$P_D(t_2) = \exp\left(-\frac{t_2}{\tau_{\mathrm{rad}}}\right). \tag{28}$$

Multiplying $P(t_1)$ with $P_D(t_2)$ gives the final relative population density at the position where the atom might emit the photon. Applying this approximation (SRM2) as opposed to the constant excitation profile (SRM1) in the analysis gives slightly different parameters of the distribution function (cf table 1). It is important to keep in mind that the analysis is, as described at the beginning of section 4, an iterative procedure that includes the LOS parallel to the normal as well.

The results of the analysis are consistent: Limiting the excitation profile to the region in front of the target removes a large portion of the population of particles, which emit in the radial direction relatively far away from the target. These particles have a large velocity in the LOS direction and, as a result, are crucial for the blue-shifted and red-shifted components. The fit compensates for this loss of particles by increasing the probability of a larger off-normal angle via decreasing the power of the cosine distribution function. The lower power of the cosine distribution gives slightly smaller energy parameters s from analyzing spectra for the LOS parallel to the normal.

An even more adequate solution is probably somewhere in between these two extreme cases. Nonetheless, the results do not differ very much, which still nicely illustrates the need to include the finite size of the target in the analysis.

5. Conclusion

A newly developed space-resolved emission model for sputtered atoms of finite-size tungsten targets was presented and benchmarked against experimental data from the linear plasma device PSI-2. In particular, the high-resolution spectra of emission by tungsten atoms sputtered from the target by Ar ions with energies of 100 eV to 140 eV were investigated. The measurements were performed using the lines of sight parallel and perpendicular to the normal of the target. The reason for developing such a model is due to unsuccessful attempts to describe the spectra of sputtered W atoms measured at the linear plasma PSI-2 using the standard ITA or the point source approximation model. ITA fails to provide consistent spectra using both lines of sight with identical energy and angular distribution function [56]. The spectra measured at the line of sight perpendicular to the normal were generally significantly broader than predicted by the ITA model. This inconsistency vanishes by analyzing the data using the SRM, whose derivation was provided in section 3.1.2. A comparison to the applied ITA model (cf section 3.2) illustrated significant differences in their line shape and showed that assuming ITA for finite-size targets may lead to an inconsistent interpretation of experimental data. Finally, the new model naturally converges to the ITA model solutions as soon as the dimensions of the target increase relative to the distance at which the emission by the atoms takes place.

Spectra simulated using different energy and angular distributions showed the expected behavior. Greater impact energies of the projectile increased the broadening, irrespective of the LOS. Changes in the angular distribution lead to opposite behavior observed for both observation angles. Naturally, this is due to the conservation of energy. Increasing the average velocity perpendicular to normal comes at the cost of decreasing the velocity parallel to the normal. Thus, the Doppler shift rises in one LOS direction but declines in the other. The parameter $s = 3.24..3.03$ for the energy and parameter $b = 0.47..0.83$ for the cosine distribution demonstrate a very good agreement with experimental spectra for the low energy range of 100 eV to 140 eV of Ar ions. Here, however, a constant excitation profile with a length of 6 cm is utilized. Assuming excitation occurs exclusively in front of the target gives parameters of the angular distribution parameter b that are reduced by

about 0.3 in all cases, whereas the energy distribution remains almost identical. The asymmetry of about 1%–2% in the experimental profiles for the LOS of 90 degrees further supports the assumption of using a step profile in the analysis. Changing the gradients of electron temperature and density, or the bias applied to the target, may drastically alter the extent of the asymmetry. So it is of utmost importance to point out that this approximation works under these conditions but may cease to be valid for other situations.

The spectra are generally remarkably well reproduced by the SRM. However, there is some room for improvement in the code. For example, the successive population increase of the tungsten metastable levels may also contribute to the remaining differences in the spectra. Furthermore, there are gradients of the plasma parameters in radial and axial direction. One should also add that the SRM model operates only in low-density limit approximation, which is valid for PSI-2 plasma. In case of higher electron densities, the ionization of excited levels will impact the line shapes.

We hope this work may stimulate more in-depth investigations on high-resolution spectroscopic studies of line shapes produced by sputtered or reflected atoms at low-temperature laboratory plasmas as it is applicable from infinite to finite-size targets. This technique can be successfully applied to test the problem of preferential sputtering, re-crystallization, or fuzz formation at the plasma surface interface. However, the complexity of the modeling can increase for plasmas with steep gradients of the plasma parameters as expression (10) ceases to be valid, and proper modeling would then require well-measured plasma parameters. Similarly, higher temperature plasmas, such as HiPIMS discharges, may be more challenging due to considerable ionization. A very high fraction of slowly-moving particles ionize since they require more time to move through the plasma before reaching the emission volume. Further refinement of the current code could prove valuable for investigating a large parameter space of sputtering under fusion-relevant conditions. For instance, near threshold-sputtering needs further investigation. The simulation of divertor-like sputtering conditions for inter-ELM phases at PSI-2 combined with using the correct model for line shape analysis is a promising candidate to probe the accuracy of the data fed into erosion simulation codes for fusion reactors. A commonly used numerical tool is the SDTrimSP code [66, 67], whose assumptions include an amorphous body and a binary collision approximation (BCA). Especially at higher energies, BCA codes demonstrate excellent agreement with experimental data [68, 69]. As an alternative, computationally more expensive molecular dynamics codes are available [70, 71]. The main uncertainty regarding these sputtering codes is in the near-threshold regime, which is typical for the inter-ELM phases. Comparing both types of codes to the experimental data would be highly interesting as it could answer the question of how reliable the simulations of the codes are for low-energy sputtering in fusion devices. PARCAS simulations indicate that exposing mono-crystalline tungsten to the plasma might be worth it, as well, due to the difference in expected dependency of the angular distribution on the crystalline orientation [72].

Acknowledgments

This work has been carried out within the framework of the EUROfusion Consortium, funded by the European Union via the Euratom Research and Training Programme (Grant Agreement No 101 052 200–EUROfusion). Views and opinions expressed are however those of the author(s) only and do not necessarily reflect those of the European Union or the European Commission. Neither the European Union nor the European Commission can be held responsible for them.

Data availability statement

All data that support the findings of this study are included within the article (and any supplementary files).

ORCID iDs

M Sackers https://orcid.org/0000-0002-5106-3373
O Marchuk https://orcid.org/0000-0001-6272-2605
S Ertmer https://orcid.org/0000-0002-8978-9567
S Brezinsek https://orcid.org/0000-0002-7213-3326
A Kreter https://orcid.org/0000-0003-3886-1415

References

[1] Anders A 2017 Tutorial: reactive high power impulse magnetron sputtering (R-HiPIMS) *J. Appl. Phys.* **121** 171101
[2] Brezinsek S *et al* 2019 Erosion, screening, and migration of tungsten in the JET divertor *Nucl. Fusion* **59** 096035

[3] Sackers M, Busch C, Tsankov Ts V, Czarnetzki U, Mertens P and Marchuk O 2022 Plasma parameters and tungsten sputter rates in a high-frequency CCP *Phys. Plasmas* **29** 043511
[4] Shishkov M and Popov D 1991 Thickness uniformity of thin films deposited on a flat substrate by sputtering of a target with rotational symmetry *Vacuum* **42** 1005–8
[5] Biel W *et al* 2019 Diagnostics for plasma control–From ITER to DEMO *Fusion Eng. Des.* **146** 465–72
[6] Brown N P and Walker M L R 2020 Review of plasma-induced hall thruster erosion *Applied Sciences* **10** 3775
[7] Kelly P J and Arnell R D 2000 Magnetron sputtering: a review of recent developments and applications *Vacuum* **56** 159–72
[8] Martynenko Y V, Rogov A V and Shul'ga V I 2012 Angular distribution of atoms during the magnetron sputtering of polycrystalline targets *Tech. Phys.* **57** 439–44
[9] Moser L, Marot L, Eren B, Steiner R, Mathys D, Leipold F, Reichle R and Meyer E 2015 Towards plasma cleaning of ITER first mirrors *Nucl. Fusion* **55** 063020
[10] Mertens P 2019 The core-plasma cxrs diagnostic for iter: an introduction to the current design *J. Fusion Energy* **38** 264–82
[11] Wehner G K 1955 Sputtering of metal single crystals by ion bombardment *J. Appl. Phys.* **26** 1056–7
[12] Knudsen M 1917 Die Verdampfung von kristalloberflächen *Ann. Phys.* **357** 105–8
[13] Thompson M W, Farmery B W and Newson P A 1968 I. A mechanical spectrometer for analysing the energy distribution of sputtered atoms of copper or gold *Philos. Mag.* **18** 361–76
[14] Sigmund P 1969 Theory of sputtering. i. sputtering yield of amorphous and polycrystalline targets *Phys. Rev.* **184** 383–416
[15] Behrisch R (ed) 2007 *Sputtering by Particle Bombardment: Experiments and Computer Calculations from Threshold to MeV Energies, vol 110 of Topics in Applied Physics* (Springer-Verlag GmbH)
[16] Bay H L 1986 Laser induced fluorescence as a technique for investigations of sputtering phenomena *Nucl. Instrum. Methods Phys. Res., Sect. B* **18** 430–45
[17] Wright R B, Pellin M J, Gruen D M and Young C E 1980 Laser fluorescence spectroscopy of sputtered uranium atoms *Nucl. Instrum. Methods* **170** 295–302
[18] Wright R B, Pellin M J and Gruen D M 1981 Velocity distribution of sputtered Zr atoms as determined by laser induced fluorescence spectroscopy *Surf. Sci.* **110** 151–78
[19] Pellin M J, Wright R B and Gruen M D 1981 Laser fluorescence spectroscopy of sputtered zirconium atoms *J. Chem. Phys.* **74** 6448–57
[20] Thompson M W and Nelson R S 1962 Evidence for heated spikes in bombarded gold from the energy spectrum of atoms ejected by 43 kev a + and xe + ions *Philos. Mag.* **7** 2015–26
[21] Thompson M W II 1968 The energy spectrum of ejected atoms during the high energy sputtering of gold *Philos. Mag.* **18** 377–414
[22] Szymoáski M and de Vries A E 1981 Beam induced decomposition and sputtering of LiI *Radiat. Eff.* **54** 135–9
[23] Stuart R V and Wehner G K 1962 Sputtering yields at very low bombarding ion energies *J. Appl. Phys.* **33** 2345–52
[24] Stuart R V, Brower K and Mayer W 1963 Time-of-flight method of determining velocities of sputtered atoms *Rev. Sci. Instrum.* **34** 425–9
[25] Oechsner H and Reichert L 1966 Energies of neutral sputtered particles *Phys. Lett.* **23** 90–2
[26] Ramos R, Cunge G, Touzeau M and Sadeghi N 2008 Measured velocity distribution of sputtered Al atoms perpendicular and parallel to the target *J. Phys. D: Appl. Phys.* **41** 152003
[27] Held J, Hecimovic A, von Keudell A and Schulz-von der Gathen V 2018 Velocity distribution of titanium neutrals in the target region of high power impulse magnetron sputtering discharges *Plasma Sources Sci. Technol.* **27** 105012
[28] Held J, Thiemann-Monjé S, von Keudell A and Schulz-von der Gathen V 2020 Velocity distribution of metal ions in the target region of HiPIMS: the role of Coulomb collisions *Plasma Sources Sci. Technol.* **29** 125003
[29] Ertmer S, Marchuk O, Dickheuer S, Brezinsek S, Boerner P, Schmitz J and Kreter A 2021 Measurements of the energy distribution of W atoms sputtered by low energy Ar ions using high-resolution Doppler spectroscopy *Plasma Phys. Controlled Fusion* **63** 015008
[30] Dickheuer S *et al* 2018 In situ measurements of the spectral reflectance of metallic mirrors at the Hα line in a low density Ar-H plasma *The Review of Scientific Instruments* **89** 063112
[31] Carter G, Fischer G, Webb R, Dzioba S, Kelly R and Auciello O 1979 On the surface-normal energy distribution of sputtered recoils *Radiat. Eff.* **45** 45–8
[32] Hintz E, Rusbüldt D, Schweer B, Bohdansky J, Roth J and Martinelli A P 1980 The determination of the flux density of sputtered atoms by means of pulsed dye laser excited fluorescence *J. Nucl. Mater.* **93-94** 656–63
[33] Bay H L, Berres W and Hintz E 1982 Surface normal velocity distribution of sputtered Zr-atoms for light-ion irradiation *Nucl. Instrum. Methods Phys. Res.* **194** 555–9
[34] Kreter A, Brandt C, Huber A, Kraus S, Möller S, Reinhart M, Schweer B, Sergienko G and Unterberg B 2015 Linear plasma device PSI-2 for plasma-material interaction studies *Fusion Sci. Technol.* **68** 8–14
[35] Linsmeier C, Unterberg B, Coenen J W, Doerner R P, Greuner H, Kreter A, Linke J and Maier H 2017 Material testing facilities and programs for plasma-facing component testing *Nucl. Fusion* **57** 092012
[36] Ertmer S, Marchuk O, Dickheuer S, Rasiński M, Kreter A and Brezinsek S 2020 Light-reflection-induced changes in the line shape of sputtered atoms *Phys. Scr.* **T171** 014031
[37] Ryde N 1976 *Atoms and Molecules in Electric Fields* (Almqvist & Wiksell International)
[38] Cowan R D 1981 *The Theory of Atomic Structure and Spectra, vol 3 of Los Alamos Series in Basic and Applied Sciences* (Univ. of California Press)
[39] Kunze H-J 2009 *Introduction to Plasma Spectroscopy, vol 56 of Springer Series on Atomic, Optical, and Plasma Physics* (Springer)
[40] Anders A, Andersson J and Ehiasarian A 2007 High power impulse magnetron sputtering: Current-voltage-time characteristics indicate the onset of sustained self-sputtering *J. Appl. Phys.* **102** 113303
[41] Drake G 2006 *Springer Handbook of Atomic, Molecular, and Optical Physics: With 111 Tables* (Springer)
[42] Falcone G 1987 Theory of collisional sputtering *Surf. Sci.* **187** 212–22
[43] Kenmotsu T, Yamamura Y, Ono T and T Kawamura 2004 A new formula for energy spectrum of sputtered atoms due to low-energy light ions *Journal of Plasma and Fusion Research* **80** 406–9
[44] Sanders J B 1968 On penetration depths and collision cascades in solid materials *PhD Thesis* Leiden University, Leiden (https://lorentz.leidenuniv.nl/IL-publications/dissertations/sources/Sanders_1968.pdf)
[45] Stepanova M and Dew S K 2001 Estimates of differential sputtering yields for deposition applications *Journal of Vacuum Science & Technology A: Vacuum, Surfaces, and Films* **19** 2805
[46] Yamamura Y, Mizuno Y and Kimura H 1986 Angular distributions of sputtered atoms for low-energy heavy ions, medium ions and light ions *Nucl. Instrum. Methods Phys. Res., Sect. B* **13** 393–5
[47] Thompson M W 1986 The velocity distribution of sputtered atoms *Nucl. Instrum. Methods Phys. Res., Sect. B* **18** 411–29

[48] Ertmer S, Marchuk O, Pospieszczyk A, Kreter A and Brezinsek S 2018 Ground state population of sputtered tungsten atoms by peak emission analysis in PSI-2 argon plasmas *Conference proceeding XLV EPS Conference on Plasma Physics* P5.1024
[49] Fujimoto T 2004 *Plasma Spectroscopy, vol 123 of International Series of Monographs on Physics* (Clarendon Press)
[50] Kramida A and Ralchenko Y 2022 Atomic spectra database *NIST Standard Reference Database 78* (https://doi.org/10.18434/T4W30F)
[51] Steinbrink J 1997 *Diploma Thesis* Humboldt-Universität Berlin
[52] Schlummer T *et al* 2017 Experimental data on low energy electron impact ionisation of W *Phys. Scr.* **T170** 014075
[53] Dickheuer S *et al* 2019 Polarization by light reflection at metallic surfaces observed in the shape of the Balmer- α line of low density plasmas *Phys. Plasmas* **26** 073513
[54] Zhu G, Sun J, Guo X, Zou X, Zhang L and Gan Z 2017 Numerical analysis of thickness uniformity of thin film deposited by rectangular planar target *2017 XVIII International Conference on Electronic Packaging Technology (ICEPT). IEEE* pp 1356–60
[55] Bishop N 2019 Thickness distribution of sputtered films on curved substrates for adjustable x-ray optics *Journal of Astronomical Telescopes, Instruments, and Systems* **5** 1
[56] Ertmer S 2022 High-resolution spectroscopy studies on sputtered atoms in the linear plasma device PSI-2 *PhD Thesis* Ruhr-Universität Bochum, Bochum
[57] Marchuk O, Brandt C, Pospieszczyk A, Reinhart M, Brezinsek S, Unterberg B and Dickheuer S 2018 Emission of fast hydrogen atoms at a plasma-solid interface in a low density plasma containing noble gases *J. Phys. B: At. Mol. Opt. Phys.* **51** 025702
[58] Ertmer S, Marchuk O, Sackers M, Dickheuer S, Brezinsek S, Mertens P and Kreter A 2020 Optical isolation of spectral lines emitted by sputtered tungsten in a weakly magnetized plasma *J. Phys. B: At. Mol. Opt. Phys.* **54** 025401
[59] Babkina T, Gans T and Czarnetzki U 2005 Energy analysis of hyperthermal hydrogen atoms generated through surface neutralisation of ions *Europhysics Letters (EPL)* **72** 235–41
[60] Yamamura Y, Takiguchi T and Ishida M 1991 Energy and angular distributions of sputtered atoms at normal incidence *Radiat. Eff. Defects Solids* **118** 237–61
[61] Goehlich A, Niemöller N and Döbele H F 1999 Determination of angle resolved velocity distributions of sputtered tungsten atoms *J. Nucl. Mater.* **266-269** 501–6
[62] Oyarzabal E, Yu J H, Doerner R P, Tynan G R and Schmid K 2006 Molybdenum angular sputtering distribution under low energy xenon ion bombardment *J. Appl. Phys.* **100** 063301
[63] Nishijima D, Baldwin M J, Doerner R P and Yu J H 2011 Sputtering properties of tungsten 'fuzzy' surfaces *J. Nucl. Mater.* **415** S96–9
[64] Eksaeva A, Marenkov E, Borodin D, Kreter A, Reinhart M, Kirschner A, Romazanov J, Terra A, Brezinsek S and Nordlund K 2017 ERO modelling of tungsten erosion in the linear plasma device PSI-2 *Nuclear Materials and Energy* **12** 253–60
[65] Marenkov E, Nordlund K, Sorokin I, Eksaeva A, Gutorov K, Jussila J, Granberg F and Borodin D 2017 Angular and velocity distributions of tungsten sputtered by low energy argon ions *J. Nucl. Mater.* **496** 18–23
[66] Mutzke A, Schneider R, Eckstein W, Dohmen R, Schmid K, von Toussaint U and Badelow G 2019 SDTrimSP Version 6.00 *Garching: Max-Planck-Institut für Plasmaphysik*
[67] Romazanov J *et al* 2017 First ERO2.0 modeling of Be erosion and non-local transport in JET ITER-like wall *Phys. Scr.* **T170** 014018
[68] Hofsäss H, Zhang K and Mutzke A 2014 Simulation of ion beam sputtering with SDTrimSP, TRIDYN and SRIM *Appl. Surf. Sci.* **310** 134–41
[69] Arredondo R, Oberkofler M, Schwarz-Selinger T, von Toussaint U, Burwitz V V, Mutzke A, Vassallo E and Pedroni M 2019 Angle-dependent sputter yield measurements of keV D ions on W and Fe and comparison with SDTrimSP and SDTrimSP-3D *Nuclear Materials and Energy* **18** 72–6
[70] Ghaly M, Nordlund K and Averback R S 1999 Molecular dynamics investigations of surface damage produced by kiloelectronvolt self-bombardment of solids *Philos. Mag.* A **79** 795–820
[71] Thompson A P *et al* 2022 LAMMPS—a flexible simulation tool for particle-based materials modeling at the atomic, meso, and continuum scales *Comput. Phys. Commun.* **271** 108171
[72] Jussila J, Granberg F and Nordlund K 2018 Effect of random surface orientation on W sputtering yields *Nuclear Materials and Energy* **17** 113–22